ORIGINAL PAPER

Influence of Defects in Graphene-Like Network of Diamond-Like Carbon on Silica Scale Adhesion

Y. Nakashima[1] · N. Umehara[2] · H. Kousaka[3] · T. Tokoroyama[2] · M. Murashima[4] · K. Murakami[1]

Abstract

Silica scale adhesion onto geothermal power plant equipment reduces the power efficiency. In our previous study, diamond-like carbon (DLC) coatings with low sp^2 fractions and high hydrogen contents were found to suppress silica adhesion. Therefore, the present study was aimed at clarifying the mechanism of silica adhesion onto the graphene-like network of DLC. In-lens scanning electron microscopic imaging of silica adhered onto defective graphene indicated that the adhesion occurred on defects in the graphene-like network. First-principles calculations revealed that the graphene with hydrogen-terminated defects exhibited reduced adsorption energy between silica and the graphene-like network. Overall, the simulations and experiments helped establish a silica adhesion model in which defects in the graphene-like network of DLC behave as silica adhesion sites.

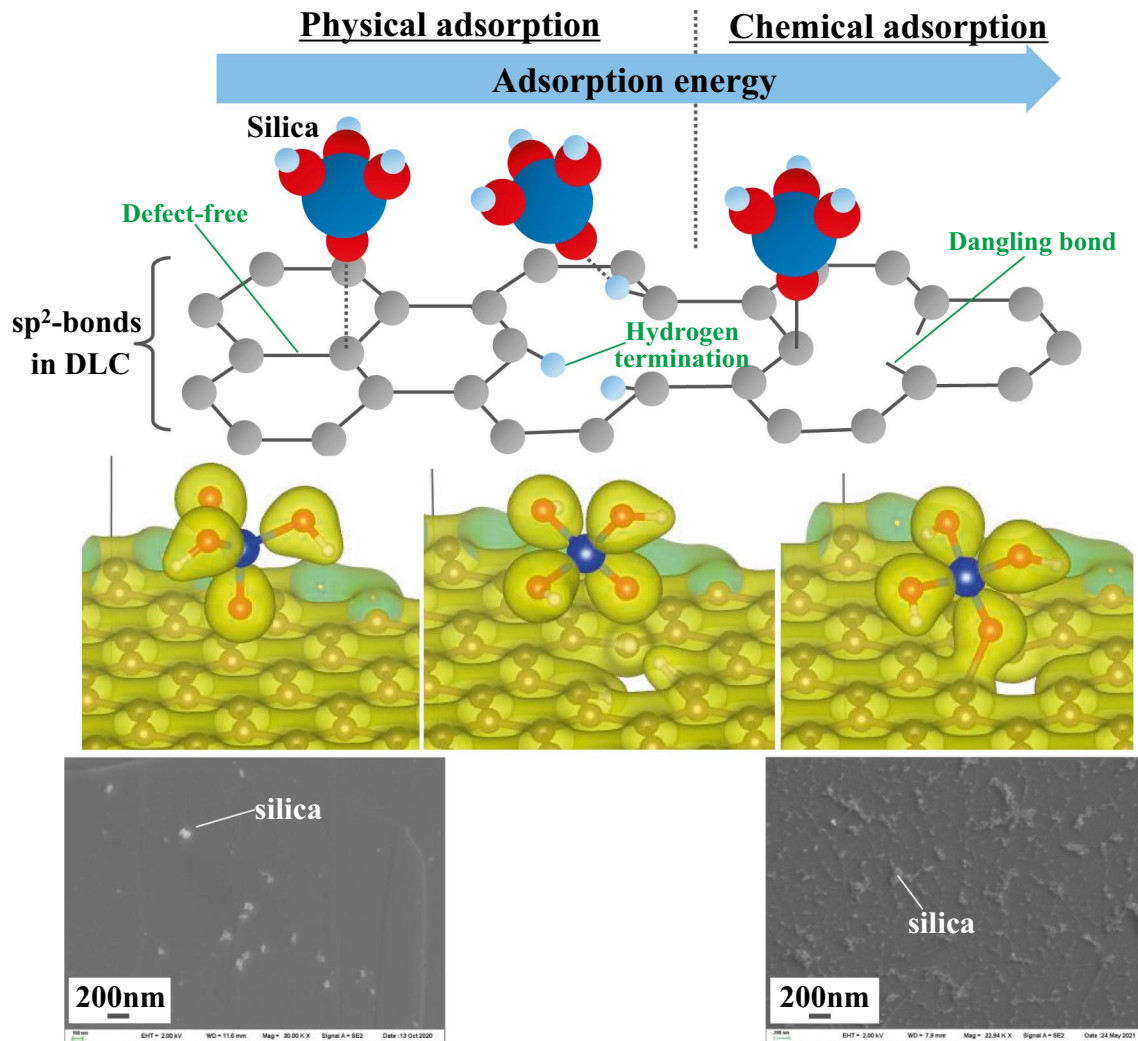✉ Y. Nakashima
  nakashima-yuuya@fujielectric.com

1   Fuji Electric Co., Ltd., Fuji-Machi, Hino 191-8502, Japan

2   Nagoya University, Furo-Cho, Chikusa-Ku,
    Nagoya 464-8603, Japan

3   Gifu University, Gifu 501-1193, Japan

4   Tohoku University, Sendai 980-8579, Japan

Graphical Abstract

1 Introduction

Geothermal power plants produce green energy because they emit 33–83 times less CO_2 than that of fossil fired thermal power plants [1, 2]. Additionally, geothermal power plants can provide a stable supply of electricity [2] in contrast to green alternatives such as solar and wind power, which are influenced by weather. Therefore, geothermal power generation is expected to be a base load green power source in the carbon–neutral era. However, geothermal steam contains a large amount of dissolved silica, which precipitates and the surfaces of power generation facilities. The silica precipitation eventually reduces the power generation efficiency because the accumulated silica reduces the geothermal steam flow paths inside

the power generation facilities [3, 4]. Physical methods for precipitated silica removal [5], such as sandblasting, and water jets, or chemical methods such as hydrofluoric acid cleaning are routinely adopted to mitigate this issue; however, power plants are typically shut down for these operations. Therefore, a method to suppress silica adhesion without power plant shutdowns is required.

Nakashima et al. recommended using diamond-like carbon (DLC) coatings with low sp^2 fractions, which is defined as ratio of $sp^2/(sp^2 + sp^3)$, and high hydrogen contents to limit silica adhesion [6]. Therefore, the use of DLC coatings could be effective in suppressing the silica adhesion without power plant shutdowns. It can save huge cost of plant shutdowns and removal method such as water jets, compared to applying DLC coating.

DLC is a carbon-based amorphous thin film with diamond- and graphite-like structures with sp^3 and sp^2-hybridization state, respectively [7]; moreover, it is resistant to corrosion and wear [8, 9] and exhibits a low friction coefficient in non-lubricant systems [10–15]. So, it is expected to experience low interaction forces with mating materials, and low adhesion performance in the case of silica scale may be expected. DLC can be categorized as hydrogen-free and hydrogen-containing DLC; these are designated as amorphous carbon (a-C) or tetrahedral amorphous carbon (ta-C) and a-C:H, respectively [6]. The ta-C coatings are excellent hard material which provide anti-wear properties [16–21]. On the other hand, ta-C coatings contain many defects (droplet) due to the physical vapor deposition (PVD) method, which trigger the wear, cracking, and thermal degradation [22–24]. Murashima et al. revealed that nitrogen-containing ta-C coatings have lower surface energy, resulting in few adhesion between ceramic particles and the ta-C coatings [25]. The coatings are known to develop unique tribolayer derived from oil additives, providing low friction and low wear tribofilms [26–29]. The a-C:H coatings are generally deposited by chemical vapor deposition (CVD) method, showing lower hardness, carbon diffusion during friction, and less chemical stability due to its graphite-rich carbon structure [27–30]. The carbonaceous structure is considered to easy to react with additive molecules on the surface, developing thick tribofilm or bring severe chemical wear of the coating [31–37]. About the adhesion on the surface it was reported that high hardness and low r energy coatings was able to demonstrate low adhesion of ceramics particles [25]. In addition, it was revealed that the surface adhesion and tribological properties could be controlled by texturing and electrical charge [38–45].

A few studies have been conducted on the adhesion behavior of silica onto DLC coatings. However, many of these have focused on biocompatibility analysis, such as adhesion to blood cells. In particular, several studies have suggested optimizing the structure of DLC using its sp^3/sp^2 ratio. Pandiyaraj et al. [46] investigated a-C:H with different sp^3/sp^2 ratios (0.9–1.0) and found that increasing the sp^3/sp^2 ratio led to increased thrombus formation, indicating an increase in the blood cell adhesion. Logothetidis [47] altered the sp^3 content of a-C and a-C:H from 20 to 80% and found that the thrombus formation was reduced and blood cell adhesion was suppressed at sp^3 contents of 40%–45%. Moreover, a significant difference in blood compatibility was observed for the same sp^3 content (40–45%), depending on the voltage bias during a-C:H deposition. Therefore, although DLC coating has same sp^3 content, adhesion property can be differed. It indicates that there are other adhesion factors besides sp^3 or sp^2 fraction derived from the structure of the DLC coatings. However, the optimal sp^2 fraction differs for various DLC types, deposition process, and deposition conditions.

Nakashima et al. investigated a-C:H and ta-CNx which is nitrogen doped ta-C, that had sp^2 fractions of 0.13–0.40 and hydrogen contents of 45–47% on the outermost surface, which were estimated by X-ray adsorption fine structure spectroscopy and elastic recoil detection analysis, respectively. Figure 1 shows the relationship between the sp^2 fraction and the amount of adhered silica in our previous study [6]. ta-CNx is hydrogen-free DLC and a-C:H is DLC with 45–47% hydrogen content. The value of adhered silica amount 1.0 indicates adhered silica amount onto uncoated specimen. In both ta-CNx and a-C:H, there is a correlation between the sp^2 fraction and the amount of adhered silica; specifically, the amount of adhered silica decreases with decreasing sp^2 fraction. Moreover, in a-C:H, the amount of adhered silica is low even when the sp^2 fraction is larger than that of ta-CNx. Therefore, it is presumed that the increased hydrogen content suppresses silica adhesion. From these results, it is clarified experimentally that reducing the sp^2 fraction and increasing the hydrogen content in DLC reduce the adhered silica amount in our previous study. Additionally, ta-CNx and a-C:H were also confirmed to have 1.0×10^{17} to 1.0×10^{20} cm^{-3} of dangling bonds by electron spin resonance (ESR) analysis in our previous study [6]. Therefore, we considered the hypothesis that dangling bonds in graphene-like network in DLC become silica adhesion sites and reducing sp^2 fraction leads to reducing dangling bond amount and hydrogen can terminates dangling bonds, then silica adhesion can be suppressed. According to the above hypothesis, the graphene-like network in DLC, which is consists predominantly of carbon atoms in the sp^2-hybridization state, could include sites for adhesion such as dangling bonds. Moreover, it is not clear whether the adhesion properties of silica are directly affected by
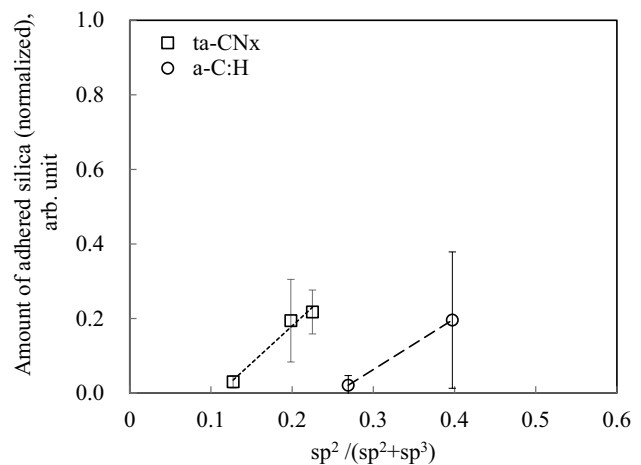

Fig. 1 Reduction of silica adhesion by decreasing sp^2 fraction [6]

the graphene-like network or by defects derived from the graphene-like network.

Therefore, to clarify the nature of the silica adhesion sites in graphene-like networks, silica was precipitated and adhered onto chemical vapor deposition (CVD)-synthesized graphene (denoted as CVD graphene) and highly oriented pyrolytic graphite (HOPG) in the present study; analysis of CVD graphene and HOPG, which represented defect-containing and defect-free graphene-like networks, respectively, helped reveal the differences in their adhered silica distributions. First-principles calculations were subsequently performed using the defect-containing and defect-free graphene sheets. The adsorption energies between silica and graphene were then calculated. The obtained results helped identify the silica adhesion sites in the graphene-like network and elucidated the mechanism of silica adhesion onto the DLC surface.

2 Experimental Section

2.1 Graphene Specimens and Structural Analysis

To confirm the influence of defects in the graphene-like network on silica adhesion, HOPG and CVD-synthesized monolayer graphene were investigated as simplified model of DLCs with defect-free and defect-containing graphene-like networks, respectively. The nascent surface of HOPG was exposed by exfoliating carbon-tape-affixed HOPG (438HP-AB; Alliance Biosystems Inc.). The CVD-synthesized monolayer graphene (CVD-GRAPH-BN-SiO$_2$-4P) was prepared by Alliance Biosystems Inc.. This specimen was obtained by transferring single-layer graphene and hexagonal boron nitride (h-BN) formed on a copper foil by CVD to a silicon wafer (100) [48–51], with the outermost layer being monolayer graphene. Raman spectroscopy (HR800, HORIBA) was performed at an excitation wavelength of 633 nm using a spot diameter of ~ 3 μm to confirm the presence or absence of defects in HOPG and CVD graphene. Field-emission scanning electron microscopy (FE-SEM; Sigma VP, Zeiss) was performed to examine the morphology and distribution of the adhered silica. Moreover, secondary electron (SE) and in-lens SE detectors were used with the FE-SEM equipment to examine the silica–graphene adhesion morphology.

In-lens detection is a technique that can determine work function differences in graphene as image contrast [52]. The work function of HOPG is known to increase with exposure to argon plasma which breaks graphene-like network, it was defined as defected-HOPG [53]. Consequently, the work function of graphene presumably increases with increasing number of defects derived from the graphene-like network. Therefore, the defects derived from the graphene-like network were expected to be visualized by in-lens FE-SEM detection, which could confirm the correlations between the adhered silica sites and the defects derived from the graphene-like network.

2.2 Silica Adhesion Tests

To examine the morphology of the adhered silica on graphene, an adhered silica specimen emulating that formed on an actual industrial equipment was precipitated and adhered from a geothermal-brine-mimicking solution. Table 1 lists the chemical composition of the imitated geothermal brine, and Fig. 2 shows a schematic of the silica adhesion test. The chemical components of the duplicated geothermal brine were derived from a previous report on silica polymerization in geothermal brine [54]. To analyze the adhered silica at the earliest stage, the HOPG and CVD graphene samples were dipped in the imitated geothermal brine for a short duration (1 h) at 50 °C. Then, the HOPG and CVD graphene with
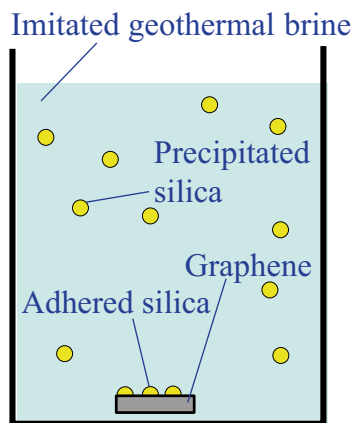

Fig. 2 Schematic illustration of the silica adhesion test

Table 1 Conditions used for silica adhesion tests			
Imitated geothermal brine	Chemical components		NaSiO$_3$·9H$_2$O (40 mmol/L)
			NaCl (200 mmol/L)
	pH		8.5 (adjusted with HCl)
Silica precipitation	Temperature (°C)		50
	Duration (h)		1
Washing	Duration (min)		1

adhered silica were washed with flowing water. The residual silica on the graphene was considered to be adhered at the earliest stage and subsequently investigated.

2.3 First-Principles Calculations of Adsorption Energy Between a Silicic Acid Ion and a Defect-Containing Graphene Sheet

To clarify the adhesion between silica and several states of graphene with defects derived from graphene-like networks, first-principles calculations of the adsorption energy were performed. First-principles calculation was widely used to reveal the adhesion and electrical properties of carbon materials [55–58]. The calculations were focused on graphene sheets with a six-membered-ring geometry and silicic acid ions.

Defects derived from the graphene-like network were introduced by extracting one carbon atom from the six-membered rings of the graphene sheets. This calculation model has three dangling bonds in the six-membered ring from which the carbon atom was extracted. Additionally, to clarify the suppression mechanism of silica adhesion at DLC coating with high hydrogen content, calculation of the adsorption energy between hydrogen-terminated graphene and silica was performed by using the dangling bonds in the six-membered rings of the graphene-like network were terminated with hydrogen. Therefore, the following three models were established for the calculations: defect-free graphene sheets, graphene sheets with defects derived from the graphene-like network owing to dangling bonds, and graphene sheets with hydrogen-terminated dangling bonds. A silicic acid ion was adsorbed onto the graphene sheet models because silica scale is deposited and adheres to equipment owing to the polymerization of silicic acid, and silicic acid ions exist at the pH of the solution used for the silica adhesion tests [59]. Consequently, silicic acid ions are considered to exhibit a stronger adsorption force than that of silicic acid owing to their charges. The energy corresponding to the adsorption of silicic acid ions onto the graphene sheet models was calculated as follows:

$$\Delta E = E_{\mathrm{ad}} - \left(E_{\mathrm{g}} + E_{\mathrm{s}} \right),$$

where ΔE is the adsorption energy, E_{ad} is the energy after the adsorption of a silicic acid ion onto the graphene sheet models, E_{g} is the energy of the graphene sheet models, and E_{s} is the energy of the silicic acid ion. In the calculations, the O atom in the silicic acid ion and C atom of graphene were initially separated by ~ 1.7 Å, and structural relaxation was performed for all atoms of the silicic acid ion. However, the structural relaxation was performed in the calculation of E_{g} for the graphene sheet with hydrogen terminations. Then, the difference between E_{ad} and $(E_{\mathrm{g}} + E_{\mathrm{s}})$ was defined

as the adsorption energy of the silicic acid ion (ΔE), which is the difference between the total energy of a silicic acid ion and graphene and the energy of the graphene and the closest silicic acid ion that is attracted to it. The distance between the graphene sheet and silicic acid ion was defined as the distance between the O⁻ of the silicic acid ion and the atom closest to the silicic acid ion, such as a C atom with a dangling bond and a H-atom-terminated dangling bond in graphene.

All electronic structure calculations were performed using plane-wave basis sets and norm-conserving pseudopotentials [60] with the Quantum Espresso code [61, 62]. The cut-off energies for the wave functions and charge density were 40 and 480 Ry, respectively, in the electronic structure calculations. The spin-unpolarized version of the generalized gradient approximation (GGA) parameterized by Perdew, Burke, and Ernzerhof [63] was used for the inter-electronic exchange–correlation function. Non-locally correlated corrections based on the van der Waals density functional (vdW-DF) [64–66] method were included. k-point sampling grids of $2 \times 2 \times 2$ and $2 \times 2 \times 1$ were used for the silicic acid ion and graphene sheet models, respectively. The occupation numbers of electrons were subjected to a smearing of 0.01 Ry using the Methfessel–Paxton method. The calculation model of the graphene sheet (Fig. 3) contained 112 carbon atoms, and the calculated cell size was $17.19 \times 17.01 \times 31.70$ Å^3. In this calculation, flat shape graphene model was adopted. On the other hand, there is possibility that graphene-like network in DLC coating has not only flat, but also curved shape, as on the surface of nano-diamonds [67]. However, a flat shape graphene model was used because there was concern that the calculation model would collapse due to the introduction of dangling bonds and hydrogen in curved graphene.

3 Results

3.1 Structural Characteristics of HOPG and CVD Graphene

To confirm the presence or absence of defects in the HOPG and CVD graphene samples, their surfaces were examined by in-lens FE-SEM detection and Raman spectroscopy. Figure 4 shows the SE and in-lens SE images of the HOPG and CVD graphene specimens, whereas Fig. 5 shows their Raman spectra.

The SE and in-lens SE images of HOPG did not reveal any differences, and the corresponding Raman spectrum showed an intense peak at 1580 cm⁻¹. Additionally, the Raman spectrum did not exhibit D bands around 1350 cm⁻¹, which are caused by defects in graphene. Therefore, the HOPG sample was confirmed to
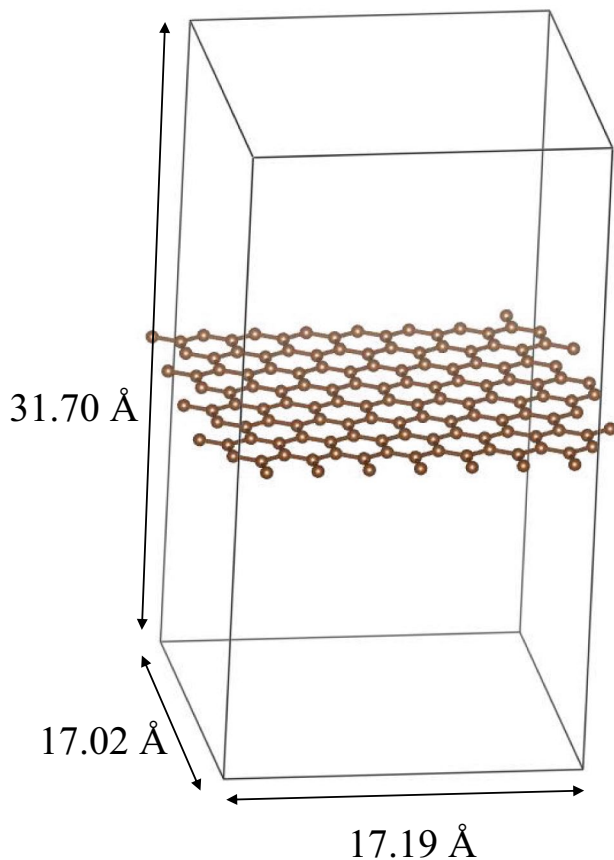
31.70 Å

17.02 Å

17.19 Å

Fig. 3 Calculation model of graphene

have a defect-free graphene network. In contrast, the in-lens SE image of the CVD graphene showed numerous black-lined patterns, although the SE image did not show any contrasting details. The hexagonal shape observed in the in-lens SE image represented bilayer graphene [49]. The higher the work function in graphene, the darker the contrast detected in the in-lens SE image [52]; therefore, the black-lined pattern represented sites with higher work functions. Additionally, the work function is known to increase with increasing exposure of the HOPG to argon plasma, indicating an increase in the number of dangling bonds in the graphene-like network [53]. Therefore, defects derived from the graphene-like network, such as dangling bonds, presumably existed along the black-lined patterns. Additionally, the Raman spectrum of the sample with the black-lined pattern showed a D band at 1350 cm^{-1}. Therefore, the black-lined pattern in CVD graphene contained defects derived from the graphene-like network. Therefore, these results indicate that defects could be identified by in-lens SE detection as contrast.

3.2 Morphologies of Silica Adhered onto HOPG and CVD-Synthesized Single-Layer Graphene

SEM observations were performed to confirm the correlation between the silica adhesion sites and the defect distributions in HOPG and CVD graphene. Figure 6 shows the SE and in-lens SE images of the HOPG and CVD graphene specimens after the silica adhesion tests.

The SE images showed silica that was several tens of nanometers in size adhered onto HOPG and CVD graphene. Moreover, the number of silica particles adhered onto CVD graphene was greater than that on HOPG. Neither dark contrast nor roughness was observed in the in-lens SE and SE images of the silica adhesion sites in HOPG, respectively. In contrast, silica selectively adhered onto CVD graphene along the black-lined pattern seen in the in-lens SE image. Therefore, silicic acid tended to preferentially adhere to defects derived from the graphene-like network. In other words, this result suggests that silica adhered selectively to graphene at defects derived from the graphene-like network, such as dangling bonds, rather than to the carbon atoms in the sp^2-hybridization state themselves.

3.3 Adsorption of Silica onto Different Graphene Models

Based on the aforementioned results of the silica adhesion tests, first-principles calculations of the adsorption energy between a silica molecule and the graphene-like network were performed to confirm whether the silica adhesion sites were determined inherently by the graphene-like network or the defects derived from the graphene-like network. Dangling bonds were artificially created as defects derived from the graphene-like network by extracting one carbon atom from the graphene-like network in the calculation model. Then, the adsorption energies of the silica molecule for the defect sites and graphene-like network were calculated. Figure 7 shows results obtained before and after the calculations of the graphene-like networks in graphene systems with no defects, with dangling bonds, and with hydrogen-terminated dangling bonds.

The atomic arrangement observed in the calculated results is described henceforth. In the defect-free graphene model, the calculated distance between the O atom in the silicic acid ion and the C atom of graphene was 2.66 Å, which is considerably greater than that in the initial arrangement (1.7 Å). However, in the graphene sheet with the dangling bond defects derived from the graphene-like network, the O^- of the silicic acid ion approached graphene, resulting in an interatomic distance of 1.59 Å between the O^- of the silicic acid ion and the C atom with the dangling bond. Additionally, the interatomic distance between the H atom
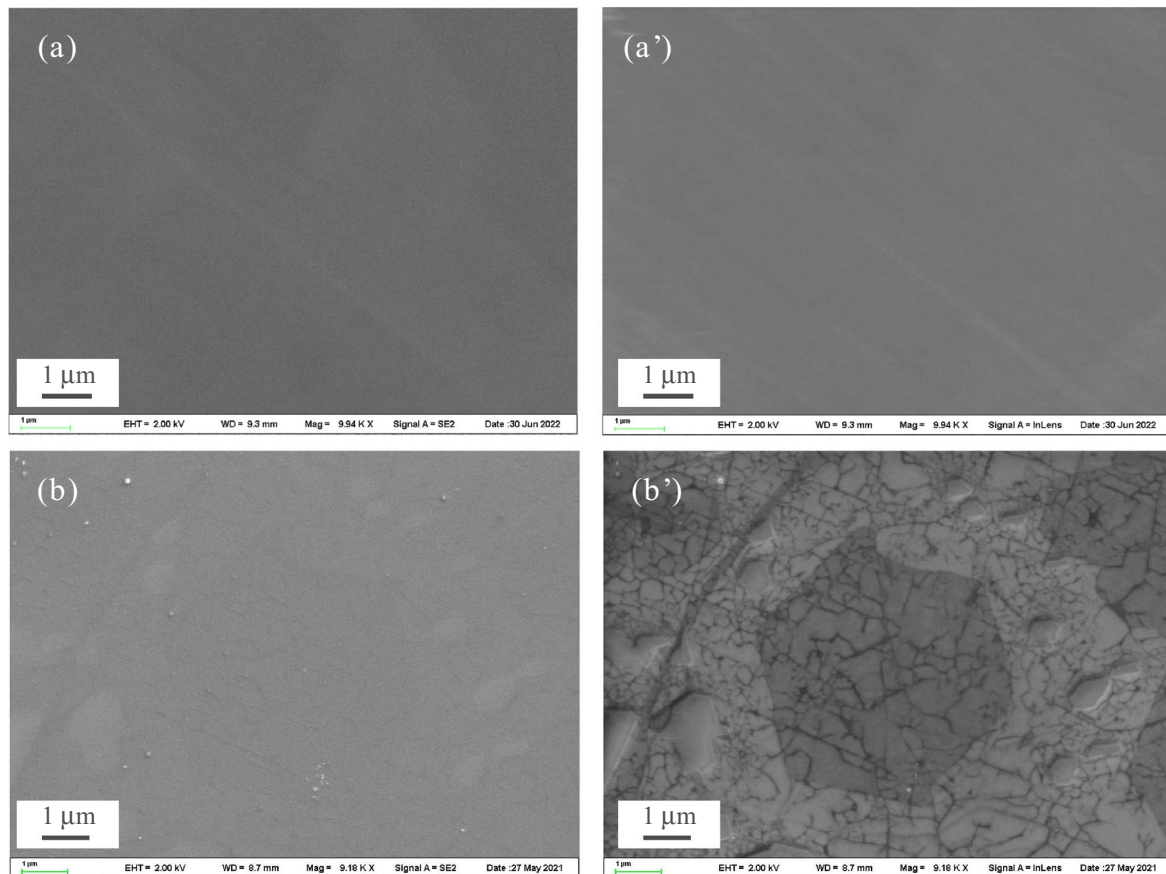
Fig. 4 SEM images of **a**, **a′** HOPG and **b**, **b′** CVD-synthesized single-layer graphene. **a**, **b** and **a′**, **b′** show SE and in-lens SE images, respectively
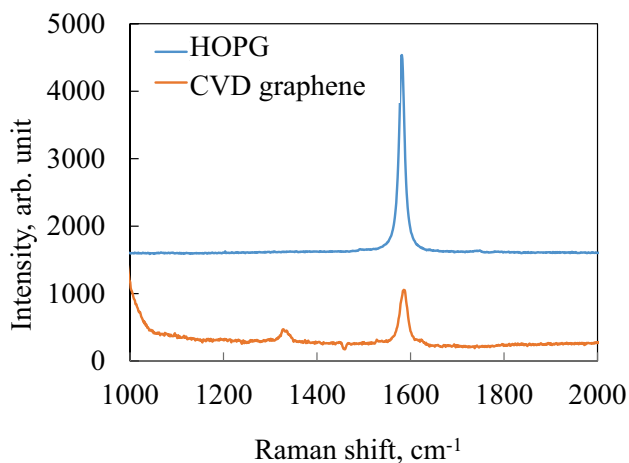

Fig. 5 Raman spectra of HOPG and CVD graphene

terminating a dangling bond of a C atom and the O^- of the silicic acid ion was 2.08 Å.

To confirm the adsorption mode of the silicic acid ion onto the graphene sheet, Bader charge [68–71] calculations were performed using the results of the respective models; the results are depicted in Fig. 8. Bader analysis is a kind of method that divides the electron density and assigns it to each atom. In this method, the electron density attributed to each atom is divided by the plane where the electron density gradient is zero. Therefore, the yellow spheres in Fig. 8 indicate the existence range of electrons in each atom. In the defect-free graphene sheet (Fig. 8a), the charge distribution between the silicic acid ions and graphene was not shared. However, in the graphene sheet with dangling bonds (Fig. 8b), the charge distribution was shared between the silicic acid ion and the dangling-bond-containing C atom, indicating the occurrence of chemical adsorption. Additionally, the charge distribution between silicic acid ions and graphene was not shared in the graphene with hydrogen-terminated dangling bonds (Fig. 8c). Therefore, physical adsorption occurred onto the defect-free and hydrogen-terminated graphene specimens. Furthermore, the graphene with dangling bonds and hydrogen-terminated possibly exhibited covalent bonding and hydrogen bonding, respectively.

The adsorption energies and modes for the investigated graphene sheet models are listed in Table 2. The absolute value of adsorption energy of graphene with dangling bonds
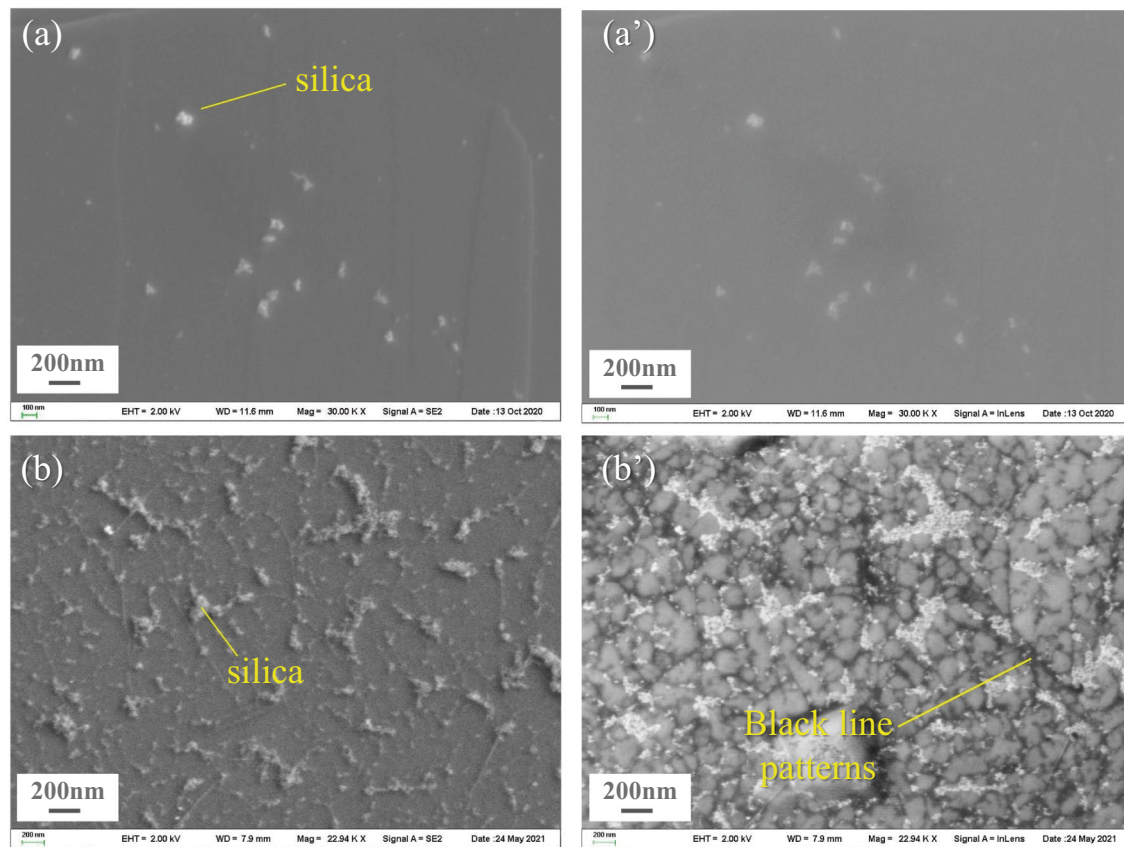
Fig. 6 Morphologies of silica adhered onto **a**, **a′** HOPG and **b**, **b′** CVD-synthesized single-layer graphene. **a**, **b** and **a′**, **b′** show SE and in-lens SE images, respectively

(-1.04 eV) was higher than that of the defect-free graphene (-0.25 eV). Therefore, a strong adsorptive force was exerted because of the high adsorption energy and the occurrence of chemical adsorption. However, the hydrogen terminations of the dangling bonds lowered the adsorption energy to -0.69 eV, and the adsorption mode changed to physical adsorption. These results indicate that although the graphene sheets with the graphene-like network did not inherently attach to the silica, defects derived from the graphene-like network, such as dangling bonds, functioned as chemisorption sites for the silica. Furthermore, by terminating the defects derived from the graphene-like network with hydrogen, the adsorption mode of silicic acid presumably changed to physical adsorption, and the adhesion of silica could be restricted. The aforementioned experimental and theoretical calculation results suggest that silica readily adhered to the defects derived from the graphene-like network, such as dangling bonds.

4 Discussion

Based on the aforementioned results, a new silica adhesion model for DLC coatings was established to address the lack of appropriate silica–DLC adhesion models. To apply DLC coatings as a low-adhesion surface for preventing silica accumulation in geothermal power plants, Nakashima et al. [6] clarified the optimal structure of DLC for suppressing silica adhesion using ta-CNx and a-C:H, which have different structures. Both ta-CNx and a-C:H were found to have reduced amounts of adhered silica with decreasing $sp^2/(sp^2 + sp^3)$ ratios in the outermost 2-nm-thick layer. Additionally, ta-CNx and a-C:H were confirmed to have 1.0×10^{17} to 1.0×10^{20} cm^{-3} of dangling bonds by electron spin resonance (ESR) analysis. Moreover, dangling bonds were found to possibly affect the
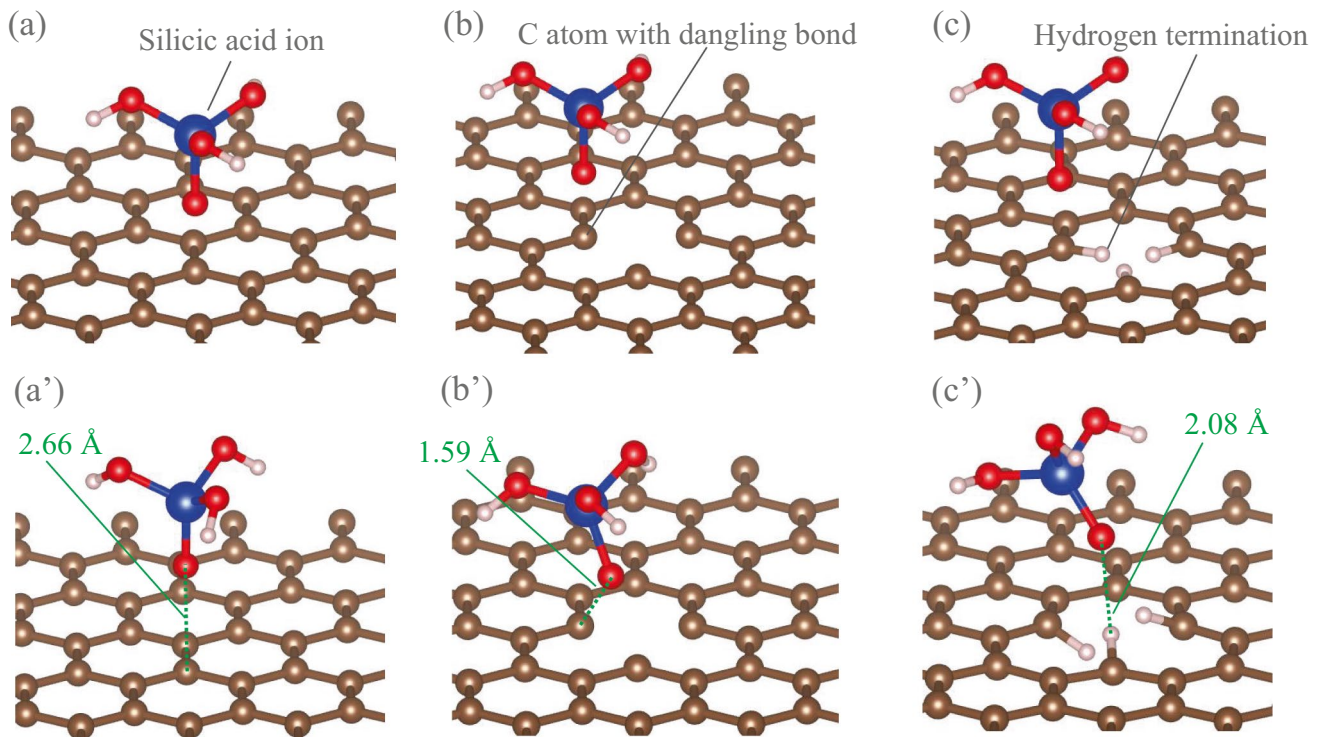
Fig. 7 Comparison of the adsorption of a silicic acid ion onto graphene **a**–**c** before and **a′**–**c′** after calculations of **a**, **a′** graphene with no defects, **b**, **b′** graphene with dangling bond defects, and **c**, **c′** graphene with hydrogen-terminated dangling bonds
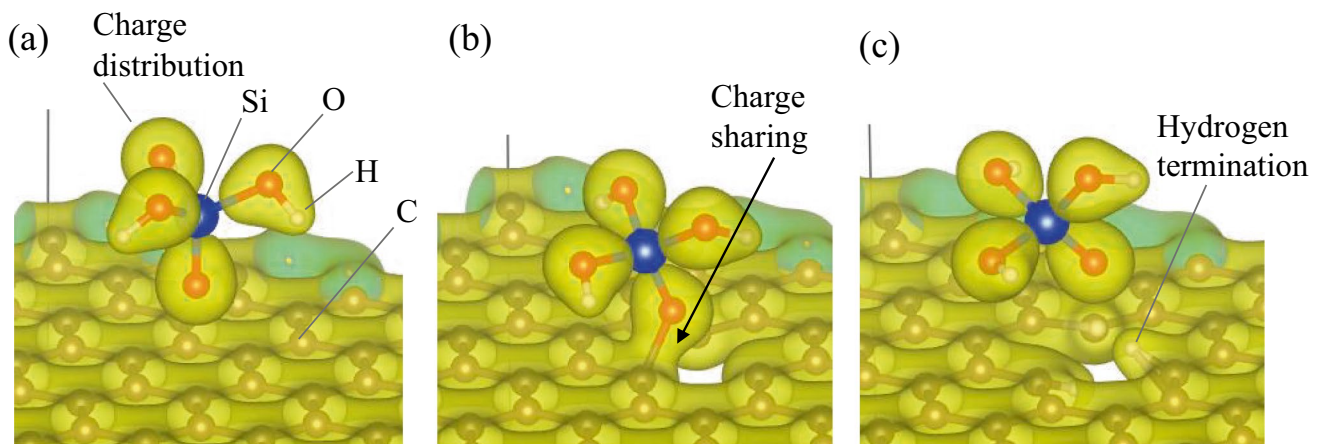

Fig. 8 Charge distributions around silicic acid ions and graphene systems **a** without defects, **b** with dangling bond defects, and **c** with hydrogen-terminated dangling bonds

Table 2 Adsorption energies and types of reaction between graphene and a silicic acid ion

Defect type	Adsorption energy (eV)	Adsorption type
Defect-free	−0.25	Physical
Dangling bonds	−1.04	Chemical
Hydrogen terminations	−0.69	Physical

silica adhesion. However, the influence of dangling bonds derived from the graphene-like network on the adhesion properties of silica was not confirmed because ESR analysis detects the number of dangling bonds for the total thickness and not for the outermost surface. According to the aforementioned results of the silica adhesion tests and first-principles calculations, the dangling bond defects derived from the graphene-like network operated as silica

adhesion sites with high adsorption energies. Therefore, decreasing the $sp^2/(sp^2 + sp^3)$ ratio in DLC could reduce the number of defects derived from the graphene-like network, consequently suppressing the amount of adhered silica. Additionally, Nakashima et al. [6] clarified that a-C:H, which contains 45–47% hydrogen, could reduce the amount of adhered silica even when the sp^2 fraction is higher than that in ta-CNx, which is free from hydrogen. In the first-principles calculations, the adsorption energy of silicic acid ions was reduced by the hydrogen terminations of the dangling bonds. Therefore, a-C:H could presumably limit the amount of adhered silica by terminating the dangling bonds in the graphene-like network with hydrogen.

The overall model of silica adhesion onto a DLC coating is illustrated in Fig. 9. Instead of the graphene-like network, the defects derived from the graphene-like network in the DLC coating become silica adhesion sites. Furthermore, these silica adhesion sites exhibited a reduced adhesion energy when the adhesion mode changed from chemical to physical adsorption through hydrogen terminations. The presence of graphene-like networks in DLC coatings may lead to defect formation and, consequently, silica adhesion sites. Therefore, finer graphene-like networks in the DLC structure could suppress adhesion. Moreover, morphology of adhered silica on DLC could be explained by silica adhesion model of Fig. 9. Figure 10 shows adhered silica morphology on ta-CNx and a-C:H. Silica adhered partly with particle morphology at ta-CNx which has lower sp^2 fraction and contains no hydrogen (Fig. 10a). In contrast, Silica adhered on whole surface with film shape and partly peeled off on a-C:H which has higher sp^2 fraction and contains high hydrogen content (Fig. 10b). These results were considered as following, ta-CNx has lower amount of dangling bond due to lower sp^2 bond fraction, so silica adhered partly as presumed silica adhesion model of Fig. 10a′. On the other hand, a-C:H has higher amount of dangling bond due to higher sp^2 bond fraction, then silica adhered on whole surface. However, it has also higher hydrogen content, then silica was tend to be peeled off due to physical adsorption between silica
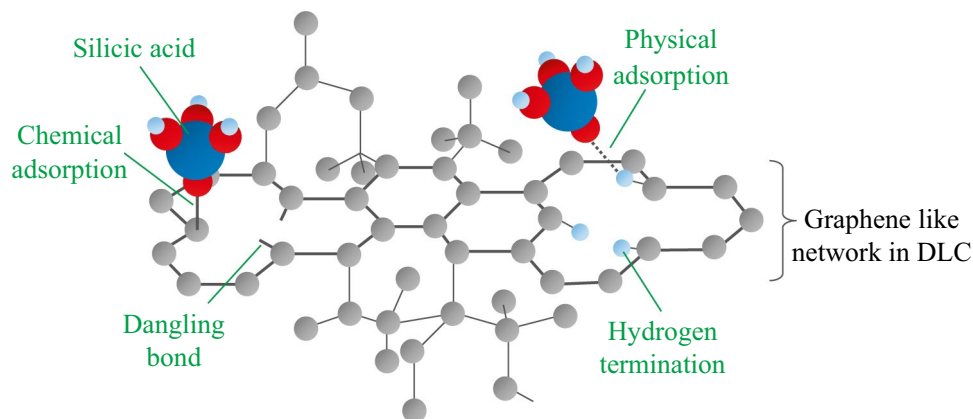
and H atom as presumed silica adhesion model of Fig. 10b′. Therefore, it is silica adhesion morphology also match to silica adsorption behavior on graphene performed by first-principle calculation.

In addition, the adhesion model illustrated in Fig. 9 could be applied to the adhesion of other substances to DLC. Pandiyaraj et al. [46] and Logothetidis [47] optimized different sp^2 fractions for studying the adherence of blood to DLC. In particular, Logothetidis [47] clarified a significant difference in blood compatibility was observed at these sp^3-bond fractions (40–45%) with respect to the presence/absence of voltage bias during the a-C:H deposition. Therefore, the amount of blood adhered presumably changed because even at the same sp^3 fractions in DLC, the presence or absence of a bias voltage during the deposition affected the amount of defects derived from the graphene-like network.

5 Conclusion

To clarify the adhesion behavior of silica onto a graphene-like network, which can help determine the amount of silica adhered to DLC coatings, an HOPG sample comprising defect-free carbon atoms in the sp^2-hybridization state and a CVD graphene specimen consisting of defective carbon atoms in the sp^2-hybridization state were used as simplified models of graphene-like networks in DLC coatings. The correlations between the defects derived from the graphene-like network and silica adhesion sites were confirmed by structural analysis of HOPG and CVD graphene as well as morphological observations of the adhered silica. Raman spectroscopy showed that the D band was absent and present in HOPG and CVD graphene, respectively. The silica adhesion tests indicated that the amount of adhered silica was higher in CVD graphene than that in HOPG. In particular, silica selectively adhered to the black-lined pattern in CVD graphene, which represented defective sites, as indicated by in-lens SE imaging with SEM. Furthermore, to clarify the adhesion of silica

Fig. 9 Model of silica adhesion onto the graphene-like network in DLC coatings
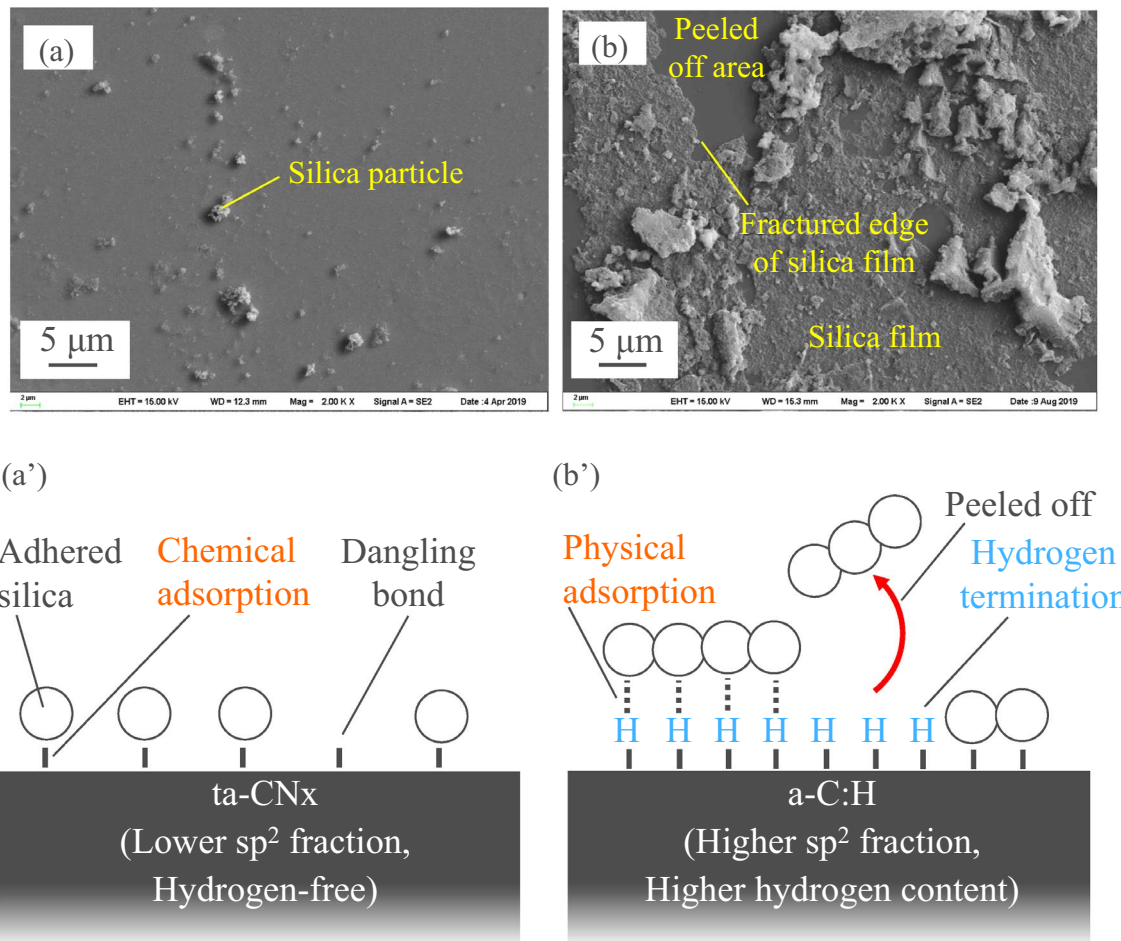
Fig. 10 Adhered silica morphology on **a** ta-CNx; sp^2 fraction 0.13 which is plot at the left end, **b** a-C:H; sp^2 fraction 0.40 and hydrogen content 47% which is plot at the right end in Fig. 1 and presumed to the defects derived from the graphene-like network, silica adhesion model at **a′** ta-CNx, **b′** a-C:H. The upper left figure (**a**) is the reprinted figure from Ref. [6]

first-principles calculations of the adsorption energies between graphene sheets comprising 112 carbon atoms and silicic acid ions were performed. The silicic acid ion was found to inherently repel the carbon atoms in the sp^2-hybridization state, and the corresponding adsorption energy was -0.25 eV. However, when dangling bonds were introduced as defects derived from the graphene-like network, the silicic acid ions chemisorbed onto the dangling bonds, increasing their adsorption energies to -1.04 eV. Introducing hydrogen terminations to the dangling bonds reduced the adsorption energy to -0.69 eV and changed the adsorption mode from chemical to physical adsorption. These results suggest that defects derived from the graphene-like network in DLC coatings become silica adhesion sites rather than the carbon atoms in the sp^2-hybridization state themselves. Moreover, the adhesion of silica could be suppressed by decreasing the number of defects by terminating them with hydrogen.

Declarations

References

1. Imamura, E., Iuchi, M., Bando, S.: Comprehensive Assessment of Life Cycle CO_2 Emissions from Power Generation Technologies in Japan. Central Research Institute of Electric Power Industry Report, p. Y06 (2016)

2. Yonekura, H.: Overview of policies on geothermal development in Japan. https://www.irena.org/-/media/Files/IRENA/Agency/Events/2013/Jan/11_4/11_Yonekura.pdf?la=en&hash=B3A8454BF076F83053364120562261A32FAF8979. Accessed 1 Aug 2022

3. Kawahara, Y., Shibata, H., Kubota, K.: Technology to counter silica scaling in binary power-generating system using geothermal hot water. Fuji Electr. Rev. **59**(2), 101–106 (2013)

4. Pambudi, N.A., Itoi, R., Jalilinasrabady, S., Gürtürk, M.: Sustainability of geothermal power plant combined with thermodynamic and silica scaling model. Geothermics **71**, 108–117 (2018). https://doi.org/10.1016/j.geothermics.2017.09.003

5. Thorhallsson, S.: Common problems faced in geothermal generation and how to deal with them. https://orkustofnun.is/gogn/unu-gtp-sc/UNU-GTP-SC-12-44.pdf. Accessed 1 Aug 2022

6. Nakashima, Y., Umehara, N., Kousaka, H., Tokoroyama, T., Murashima, M., Mori, D.: Carbon-based coatings for suppression of silica adhesion in geothermal power generation. Tribol. Int. **177**, 107956 (2023). https://doi.org/10.1016/j.triboint.2022.107956

7. Ferrari, A.C., Robertson, J.: Interpretation of Raman spectra of disordered and amorphous carbon. Phys. Rev. B **61**(20), 14095 (2000). https://doi.org/10.1103/PhysRevB.61.14095

8. Liu, X., Yamaguchi, R., Umehara, N., Deng, X., Kousaka, H., Murashima, M.: Clarification of high wear resistance mechanism of ta-CNx coating under poly alpha-olefin (PAO) lubrication. Tribol. Int. **105**, 193–200 (2017). https://doi.org/10.1016/j.triboint.2016.10.016

9. Mabuchi, Y., Higuchi, T., Yoshimura, D., Murashima, M., Kousaka, H., Umehara, N.: Influence of carbon black in engine oil on wear of H-free diamond-like carbon coatings. Tribol. Int. **73**, 138–147 (2014). https://doi.org/10.1016/j.triboint.2014.01.016

10. Erdemir, A.: The role of hydrogen in tribological properties of diamond-like carbon films. Surf. Coat. Technol. **146–147**, 292–297 (2001). https://doi.org/10.1016/S0257-8972(01)01417-7

11. Erdemir, A.: Genesis of superlow friction and wear in diamondlike carbon films. Tribol. Int. **37**, 1005–1012 (2004). https://doi.org/10.1016/j.triboint.2004.07.018

12. Murashima, M., Maeda, M., Xingrui, D., Umehara, N., Kousaka, H.: Development of a new diamond-like carbon surface treatment method with electric discharge for short running-in and friction reduction. Proc. Inst. Mech. Eng. Part J **236**(5), 1020–1030 (2021)

13. Murashima, M., Oyama, S., Kousaka, H., Tokoroyama, T., Lee, W.Y., Umehara, N.: New in situ low-friction technology for diamond-like carbon coatings using surface discharge treatment in

ambient air. Tribol. Int. **165**, 107306 (2022). https://doi.org/10.1016/j.triboint.2021.107306

14. Wu, W., Murashima, M., Saso, T., Tokoroyama, T., Lee, W.Y., Kousaka, H., Umehara, N.: New in situ superlow-friction method for nitrogen-containing diamond-like carbon coatings using dielectric barrier discharge treatment in ambient air. Tribol. Int. **174**, 107749 (2022). https://doi.org/10.1016/j.triboint.2022.107749

15. Nishimura, H., Umehara, N., Kousaka, H., Murashima, M.: Clarification of effect of transformed layer and oil film on low friction coefficient of CNx coating in PAO oil lubrication by in-situ observation of friction area with reflectance spectroscopy. Tribol. Int. **113**, 383–388 (2017)

16. Mustafa, M.M.B., Umehara, N., Tokoroyama, T., Murashima, M., Shibata, A., Utsumi, Y., Moriguchi, H.: Effect of pillar and mesh structure of tetrahedral amorphous carbon (ta-C) coatings on the wear properties and fracture toughness of the coating. Tribology **14**(5), 388–397 (2019). https://doi.org/10.2474/trol.14.388

17. Mustafa, M.M.B., Umehara, N., Tokoroyama, T., Murashima, M., Shibata, A., Utsumi, Y., Moriguchi, H.: Effect of mesh structure of tetrahedral amorphous carbon (ta-C) coating on friction and wear properties under base-oil lubrication condition. Tribol. Int. **147**, 105557 (2022). https://doi.org/10.1016/j.triboint.2019.01.016

18. Yamada, Y., Murashima, M., Umehara, N., Tokoroyama, T., Lee, W.Y., Takamatsu, H., Tanaka, Y., Utsumi, Y.: Effect of fracture properties and surface morphology on wear of DLC coatings at severe contact condition. Tribol. Int. **169**, 107486 (2022). https://doi.org/10.1016/j.triboint.2022.107486

19. Liu, X., Yamaguchi, R., Umehara, N., Murashima, M., Tokoroyama, T.: Effect of oil temperature and counterpart material on the wear mechanism of ta-CNx coating under base oil lubrication. Wear **390–391**, 312–321 (2017). https://doi.org/10.1016/j.wear.2017.08.012

20. Liu, X., Umehara, N., Tokoroyama, T., Murashima, M.: Tribological properties of ta-CNx coating sliding against steel and sapphire in unlubricated condition. Tribol. Int. **131**, 102–111 (2019). https://doi.org/10.1016/j.triboint.2018.10.022

21. Mahmud, K.A.H.A., Varman, M., Kalam, M.A., Masjuki, H.H., Mobarak, H.M., Zulkifli, H.W.M.: Tribological characteristics of amorphous hydrogenated (a-C:H) and tetrahedral (ta-C) diamond-like carbon coating at different test temperatures in the presence of commercial lubricating oil. Surf. Coat. Technol. **245**, 133–147 (2014). https://doi.org/10.1016/j.surfcoat.2014.02.052

22. Murashima, M., Deng, X., Izuoka, H., Umehara, N., Kousaka, H.: Effect of oxygen on degradation of defects on ta-C coatings deposited by filtered arc deposition. Surf. Coat. Technol. **362**, 200–207 (2019). https://doi.org/10.1016/j.surfcoat.2019.01.115

23. Lee, W.Y., Tokoroyama, T., Murashima, M., Umehara, N.: Investigation running-in behavior to understand wear behavior of ta-C coating with filtered cathodic vacuum arc deposition. J. Tribol. **23**, 38–47 (2019)

24. Lee, W.Y., Jang, Y.J., Tokoroyama, T., Murashima, M., Umehara, N.: Effect of defects on wear behavior in ta-C coating prepared by filtered cathodic vacuum arc deposition. Diam. Relat. Mater. **105**, 107789 (2020). https://doi.org/10.1016/j.diamond.2020.107789

25. Murashima, M., Hojo, K., Ito, S., Umehara, N., Tokoroyama, T., Takahashi, T., Imaeda, M.: Nanotextured mold surface with DLC coating for reduction in residual ceramic particles. Langmuir **37**, 3563–3574 (2021). https://doi.org/10.1021/acs.langmuir.0c03435

26. Li, X., Murashima, M., Umehara, N.: Effect of nanoparticles as lubricant additives on friction and wear behavior of tetrahedral amorphous carbon (ta-C) coating. J. Tribol. **16**, 15–29 (2018)

27. Aboua, K.A.M., Umehara, N., Kousaka, H., Tokoroyama, T., Murashima, M., Tasdemir, H.D., Mabuchi, Y., Higuchi, T.: Effect of ZnDTP tribofilm's morphology on friction behavior of DLC coatings: tribofilm characterization by 3D scanning electron

microscope observation. J. Adv. Mech. Des. Syst. Manuf. **12**(7), 18–00319 (2018). https://doi.org/10.1299/jamdsm.2018jamdsm0129

28. Hashizume, N., Murashima, M., Umehara, N., Tokoroyama, T., Lee, W.Y.: In situ observation of the formation of MoDTC-derived tribofilm on a ta-C coating using reflectance spectroscopy and its effects on friction. Tribol. Int. **162**, 107128 (2021). https://doi.org/10.1016/j.triboint.2021.107128

29. Lee, W.Y., Murashima, M., Umehara, N., Tokoroyama, T., Horaguchi, N., Ishimoto, T.: Realization of near-less friction of ta-CNx coating under R32 refrigerant environment. Tribol. Int. **168**, 107404 (2022). https://doi.org/10.1016/j.triboint.2021.107404

30. Li, X., Sawaki, T., Kousaka, H., Murashima, M., Umehara, N.: Effect of mating materials on wear properties of amorphous hydrogenated carbon (a-C:H) coating and tetrahedral amorphous carbon (ta-C) coating in base oil boundary lubrication condition. J. Tribol. **15**, 1–20 (2017)

31. Kosarieh, S., Morina, A., Lainé, E., Flemming, J., Neville, A.: The effect of MoDTC-type friction modifier on the wear performance of a hydrogenated DLC coating. Wear **302**, 890–898 (2013). https://doi.org/10.1016/j.wear.2012.12.052

32. Aboua, K.A.M., Umehara, N., Kousaka, H., Tokoroyama, T., Murashima, M., Mabuchi, Y., Higuchi, T., Kawaguchi, M.: Effect of carbon diffusion on friction and wear behaviors of diamond-like carbon coating against Cr-plating in boundary base oil lubrication. Tribology **13**(5), 290–300 (2018). https://doi.org/10.2474/trol.13.290

33. Aboua, K.A.M., Umehara, N., Kousaka, H., Tokoroyama, T., Murashima, M., Mabuchi, Y., Higuchi, T., Kawaguchi, M.: Effect of carbon diffusion on friction and wear behaviors of diamond-like carbon coating against germanium in boundary base oil lubrication. Tribol. Lett. **67**, 65 (2019). https://doi.org/10.1007/s11249-019-1179-2

34. Aboua, K.A.M., Umehara, N., Kousaka, H., Tokoroyama, T., Murashima, M., Mustafa, M.M.B., Mabuchi, Y., Higuchi, T., Kawaguchi, M.: Effect of mating material and graphitization on wear of a-C: H coating in boundary base oil lubrication. Tribol. Lett. **68**, 24 (2020). https://doi.org/10.1007/s11249-019-1248-6

35. Taib, M.T.B., Umehara, N., Tokoroyama, T., Murashima, M.: The effect of UV irradiation to a-C: H on friction and wear properties under PAO oil lubrication including MoDTC and ZnDTP. Tribology **13**(3), 119–130 (2018). https://doi.org/10.2474/trol.13.119

36. Kassim, K.A.M., Tokoroyama, T., Murashima, M., Umehara, N.: The wear classification of MoDTC-derived particles on silicon and hydrogenated diamond-like carbon at room temperature. Tribol. Int. **147**, 106176 (2020). https://doi.org/10.1016/j.triboint.2020.106176

37. Kassim, K.A.M., Tokoroyama, T., Murashima, M., Lee, W.Y., Umehara, N., Mustafa, M.M.B.: Wear acceleration of a-C: H coatings by molybdenum-derived particles: mixing and temperature effects. Tribol. Int. **159**, 106944 (2021). https://doi.org/10.1016/j.triboint.2021.106944

38. Etsion, I.: Improving tribological performance of mechanical components by laser surface texturing. Tribol. Lett. **17**(4), 733–737 (2004). https://doi.org/10.1007/s11249-004-8081-1

39. Murashima, M., Umehara, N., Kousaka, H.: Effect of nano-texturing on adhesion of thermoplastic resin against textured steel plate. Tribology **11**(2), 159–167 (2016). https://doi.org/10.2474/trol.11.159

40. Murashima, M., Yoshino, S., Kawaguchi, M., Umehara, N.: Intelligent tribological surfaces: from concept to realization using additive manufacturing. Int. J. Mech. Mater. Des. **15**, 757–766 (2019). https://doi.org/10.1007/s10999-018-9435-4

41. Pettersson, U., Jacobson, S.: Friction and wear properties of micro textured DLC coated surfaces in boundary lubricated sliding. Tribol. Lett. **17**(3), 553–559 (2004). https://doi.org/10.1023/B:TRIL.0000044504.76164.4e

42. He, D., Zheng, S., Pu, J., Zhang, G., Hu, L.: Improving tribological properties of titanium alloys by combining laser surface texturing and diamond-like carbon film. Tribol. Int. **82**, 20–27 (2015). https://doi.org/10.1016/j.triboint.2014.09.017

43. Murashima, M., Imaizumi, Y., Murase, R., Umehara, N., Tokoroyama, T., Saito, T., Takeshima, M.: Active friction control in lubrication condition using novel metal morphing surface. Tribol. Int. **156**, 106827 (2021). https://doi.org/10.1016/j.triboint.2020.106827

44. Murashima, M., Imaizumi, Y., Kawaguchi, M., Umehara, N., Tokoroyama, T., Saito, T., Takeshima, M., Tsukiyama, Y., Nitta, I.: Realization of a novel morphing surface using additive manufacturing and its active control in friction. J. Tribol. **143**(5), 051104 (2021). https://doi.org/10.1115/1.4050269

45. Murashima, M., Umehara, N., Kousaka, H., Deng, X.: Effect of electric field on adhesion of thermoplastic resin against steel plate. Tribology **12**(2), 42–48 (2017). https://doi.org/10.2474/trol.12.42

46. Pandiyaraj, K.N., Selvarajan, V., Heeg, J., Junge, F., Lampka, A., Barfels, T., Wienecke, M., Rhee, Y.H., Kim, H.W.: Influence of bias voltage on diamond like carbon (DLC) film deposited on polyethylene terephthalate (PET) film surfaces using PECVD and its blood compatibility. Diam. Relat. Mater. **19**(7–9), 1085–1092 (2010). https://doi.org/10.1016/j.diamond.2010.03.016

47. Logothetidis, S.: Haemocompatibility of carbon based thin films. Diam. Relat. Mater. **16**(10), 1847–1857 (2007). https://doi.org/10.1016/j.diamond.2007.05.012

48. Li, X., Cai, W., An, J., Kim, S., Nah, J., Yang, D., Piner, R., Velamakanni, A., Jung, I., Tutuc, E., Banerjee, S.K., Colombo, L., Ruoff, R.S.: Large-area synthesis of high-quality and uniform graphene films on copper foils. Science **324**(5932), 1312–1314 (2009). https://doi.org/10.1126/science.1171245

49. Liang, X., Sperling, B.A., Calizo, I., Cheng, G., Hacker, C.A., Zhang, Q., Obeng, Y., Yan, K., Peng, H., Li, Q., Zhu, X., Yuan, H., Walker, A.R.H., Liu, Z., Peng, L., Richter, C.A.: Toward clean and crackless transfer of graphene. ACS Nano **5**(11), 9144–9153 (2011). https://doi.org/10.1021/nn203377t

50. Li, X., Zhu, Y., Cai, W., Borysiak, M., Han, B., Chen, D., Piner, R.D., Colombo, L., Ruoff, R.S.: Transfer of large-area graphene films for high-performance transparent conductive electrodes. Nano Lett. **9**(12), 4359–4363 (2009). https://doi.org/10.1021/nl902623y

51. Wang, J., Ma, F., Liang, W., Sun, M.: Electrical properties and applications of graphene, hexagonal boron nitride (h-BN), and graphene/h-BN heterostructures. Mater. Today Phys. **2**, 6–34 (2017). https://doi.org/10.1016/j.mtphys.2017.07.001

52. Zhou, Y., Fox, D.S., Maguire, P., O'Connell, R., Masters, R., Rodenburg, C., Wu, H., Dapor, M., Chen, Y., Zhang, H.: Quantitative secondary electron imaging for work function extraction at atomic level and layer identification of graphene. Sci. Rep. **6**, 21045 (2016). https://doi.org/10.1038/srep21045

53. Akada, K., Terasawa, T., Imamura, G., Obata, S., Saiki, K.: Control of work function of graphene by plasma assisted nitrogen doping. Appl. Phys. Lett. **104**(13), 131602 (2014). https://doi.org/10.1063/1.4870424

54. Yoneya, M., Ikeshoji, T., Kimura, S.: Numerical analysis for experimental results in silica prevention by cathodic current method. Circ. Gov. Ind. Res. Inst. Tohoku **25**, 15–22 (1992)

55. Kinoshita, Y., Murashima, M., Kawachi, M., Ohno, N.: First-principles study of mechanical properties of one-dimensional carbon nanotube intramolecular junctions. Comput. Mater. Sci. **70**, 1–7 (2013). https://doi.org/10.1016/j.commatsci.2012.12.033

56. Mohiuddin, T.M.G., Lombardo, A., Nair, R.R., Bonetti, A., Savini, G., Jalil, R., Bonini, N., Basko, D.M., Galiotis, C., Marzari, N., Novoselov, K.S., Geim, A.K., Ferrari, A.C.: Uniaxial strain in

graphene by Raman spectroscopy: G peak splitting, Grüneisen parameters, and sample orientation. Phys. Rev. B **79**, 205433 (2009). https://doi.org/10.1103/PhysRevB.79.205433

57. Chan, K.T., Neaton, J.B., Cohen, M.L.: First-principles study of metal adatom adsorption on graphene. Phys. Rev. B **77**, 235430 (2008). https://doi.org/10.1103/PhysRevB.77.235430

58. Leenaerts, O., Partoens, B., Peeters, F.M.: Adsorption of H_2O, NH_3, CO, NO_2, and NO on graphene: a first-principles study. Phys. Rev. B **77**, 125416 (2008). https://doi.org/10.1103/PhysRevB.77.125416

59. Siga, H., Higuchi, M., Azuma, Y.: Initial stage polymerization of silicic acid in aqueous solution. Inorg. Mater. **4**(268), 223–231 (1997). https://doi.org/10.11451/mukimate1994.4.223

60. Hamann, D.R., Schlüter, M., Chiang, C.: Norm-conserving pseudopotentials. Phys. Rev. Lett. **43**(20), 1494 (1979). https://doi.org/10.1103/PhysRevLett.43.1494

61. Giannozzi, Y., Baroni, S., Bonini, N., Calandra, M., Car, R., Cavazzoni, C., Ceresoli, D., Chiarotti, G.L., Cococcioni, M., Dabo, I., Corso, A.D., de Gironcoli, S., Fabris, S., Fratesi, G., Gebauer, R., Gerstmann, U., Gougoussis, C., Kokalj, A., Lazzeri, M., Martin-Samos, L., Marzari, N., Mauri, F., Mazzarello, R., Paolini, S., Pasquarello, A., Paulatto, L., Sbraccia, C., Scandolo, S., Sclauzero, G., Seitsonen, A.P., Smogunov, A., Umari, P., Wentzcovitch, R.M.: QUANTUM ESPRESSO: a modular and opensource software project for quantum simulations of materials. J. Phys. **21**(39), 395502 (2009). https://doi.org/10.1088/0953-8984/21/39/395502

62. Giannozzi, P., Andreussi, O., Brumme, T., Bunau, O., Nardelli, M.B., Calandra, M., Car, R., Cavazzoni, C., Ceresoli, D., Cococcioni, M., Colonna, N., Carnimeo, I., Corso, A.D., de Gironcoli, S., Delugas, P., DiStasio, R.A., Jr., Ferretti, A., Floris, A., Fratesi, G., Fugallo, G., Gebauer, R., Gerstmann, U., Giustino, F., Gorni, T., Jia, J., Kawamura, M., Ko, H.-Y., Kokalj, A., Küçükbenli, E., Lazzeri, M., Marsili, M., Marzari, N., Mauri, F., Nguyen, N.L., Nguyen, H.-V., Otero-de-la-Roza, A., Paulatto, L., Poncé, S., Rocca, D., Sabatini, R., Santra, B., Schlipf, M., Seitsonen, A.P., Smogunov, A., Timrov, I., Thonhauser, T., Umari, P., Vast, N., Wu, X., Baroni, S.: Advanced capabilities for materials modelling with QUANTUM ESPRESSO. J. Phys. **29**(46), 465901 (2017). https://doi.org/10.1088/1361-648X/aa8f79

63. Perdew, J.P., Burke, K., Ernzerhof, M.: Generalized gradient approximation made simple. Phys. Rev. Lett. **77**(18), 3865 (1996). https://doi.org/10.1103/PhysRevLett.77.3865

64. Rydberg, H., Dion, M., Jacobson, N., Schroder, E., Hyldgaard, P., Simak, S.I., Langreth, D.C., Lundqvist, B.I.: Van der Waals density functional for layered structures. Phys. Rev. Lett. **91**(12), 126402 (2003). https://doi.org/10.1103/PhysRevLett.91.126402

65. Dion, M., Rydberg, H., Schroder, E., Langreth, D.C., Lundqvist, B.I.: Van der Waals density functional for general geometries. Phys. Rev. Lett. **92**(24), 246401 (2004). https://doi.org/10.1103/PhysRevLett.92.246401

66. Berland, K., Cooper, V.R., Lee, K., Schroder, E., Thonhauser, T., Hyldgaard, P., Lundqvist, B.I.: van der Waals forces in density functional theory: a review of the vdW-DF method. Rep. Prog. Phys. **78**(6), 066501 (2015). https://doi.org/10.1088/0034-4885/78/6/066501

67. Baitinger, E.M., Belenkov, E.A., Brzhezinskaya, M.M., Greshnyakov, V.A.: Specific features of the structure of detonation nanodiamonds from results of electron microscopy investigations. Phys. Solid State **54**(8), 1715–1722 (2012)

68. Tang, W., Sanville, E., Henkelman, G.: A grid-based Bader analysis algorithm without lattice bias. J. Phys. **21**(8), 084204 (2009). https://doi.org/10.1088/0953-8984/21/8/084204

69. Sanville, E., Kenny, S.D., Smith, R., Henkelman, G.: An improved grid-based algorithm for Bader charge allocation. J. Comput. Chem. **28**(5), 899–908 (2007). https://doi.org/10.1002/jcc.20575

70. Henkelman, G., Arnaldsson, A., Jónsson, H.: A fast and robust algorithm for Bader decomposition of charge density. Comput. Mater. Sci. **36**(3), 354–360 (2006). https://doi.org/10.1016/j.commatsci.2005.04.010

71. Yu, M., Trinkle, D.R.: Accurate and efficient algorithm for Bader charge integration. J. Chem. Phys. **134**, 064111 (2011). https://doi.org/10.1063/1.3553716

Publisher's Note Springer Nature remains neutral with regard to jurisdictional claims in published maps and institutional affiliations.